Citrate-Stabilized Gold Nanoparticles as High-Performance Electrocatalyst: The Role of the Size on the Electroreduction of Oxygen

David Alba-Molina,[1] Alain R. Puente Santiago,[2] Juan J. Giner-Casares,[1,] María T. Martín-Romero,[1] Luis Camacho,[1] Rafael Luque,[2] Manuel Cano[1,*]*

[1] Department of Physical Chemistry and Applied Thermodynamics, Institute of Fine Chemistry and Nanochemistry, University of Córdoba, Campus Universitario de Rabanales, Edificio Marie Curie, Córdoba, Spain E-14014

[2] Department of Organic Chemistry, Institute of Fine Chemistry and Nanochemistry, University of Córdoba, Campus Universitario de Rabanales, Edificio Marie Curie, Córdoba, Spain E-14014

Corresponding Authors

*jjginer@uco.es, q82calum@uco.es

Abstract

Fuel cells stand out as one of the most promising alternatives for non-sustainable fossil-based economy. Efficient electrocatalysts for the Oxygen Reduction Reaction (ORR) are required for the mass application of fuel cells. Citrate-stabilized gold nanoparticles (AuNPs) are proposed as potential-dependent electrocatalysts for the ORR. AuNPs were synthesized by a green, reproducible and easy scale-up method. After exhaustive characterization, the electrocatalytic activity of the resulting AuNPs was investigated in alkaline media. Static and dynamic electrochemical studies showed a core-size dependent tendency both for their potentials and intensities. For the first time ever, the hysteresis effect in the ORR profile over Au nanoelectrocatalysts is reported herein. In addition, the electrocatalytic efficiency was comparable to those obtained for Au clusters, suggesting the benefits of citrate stabilizing agent on the electrocatalyst performance of nanomaterials based on noble metals for ORR. These results pave the way for the design of non-coated AuNPs as strong candidate for ORR.

1. Introduction.

The development of effective and easily scaled-up nanomaterials which can achieve needed current densities for the fabrication of ORR cathodes electrodes for practical applications constitute one of the hottest research topic in the field of electrocatalysis in sustainable energy.[1–4] Pt-based nanomaterials have been widely investigated as active catalysts for ORR cathode reactions in the last decade owed to their highly efficient electrocatalytic properties.[5] Nevertheless, their instability as ORR electrocatalysts together with sluggish reaction dynamics and the high cost of Pt precious metal have considerably limited the wide-spread commercialization of fuel cells based on the aforementioned materials.[6] Consequently, in recent years, a number of endeavors has been focused to the developed of non-platinum nanoelectrocatalysts such as nitrogen-doped carbon nanotubes,[6] porous gold nanoparticles,[7] gold-nanoparticle/graphene as nanocomposites materials,[8] porous carbon-supported gold nanoparticles[9] or even atomically dispersed Fe–Nx species on porous porphyrinic triazine-based frameworks.[10]

Gold nanostructures are revealed as promising electrocatalytic platforms given that gold nanoclusters acts an electron transfer (ET) enhancer and their large active surface area improve the oxygen adsorption.[11–14] Gold nanoclusters have been proposed as relevant nanomaterials for electrocatalysis for the ORR.[15] The effect of the gold core size on the electrocatalytic performances was deeply addressed. Despite the afore mentioned studies, the elucidation of the electrocatalytic size dependence behavior as well as the kinetics properties of gold nanoparticles (AuNPs) with size above 10 nm has not been reported.

We propose herein a green and an easily scaled-up seeded growth method previously reported by Bastus *et al*., for the synthesis of high-quality and long-term stable citrate-stabilized AuNPs with sizes of 15 nm, 28 nm, 55 nm and 95 nm, respectively.[16,17] After exhaustive characterization,

citrate-stabilized AuNPs with different size were tested for the electroreduction of oxygen by detailed static and dynamic electrochemical measurements.

2. Experimental Methods.

2.1. Synthesis of citrate-stabilized AuNPs. 15 nm (step 2), 28 nm (step 4), 55 nm (step 8) and 95 nm (step 11) citrate-stabilized gold nanoparticles (AuNPs) with a uniform quasi spherical shape and a narrow size distribution were synthesized, by sequential manner, following a kinetically controlled seeded growth strategy via the reduction of $HAuCl_4$ by sodium citrate.[16,17] Briefly, 150 mL of 2.2 mM sodium citrate solution was heated in a 250 mL three-neck round-bottom flask for 15 min under vigorous stirring. Once the boiling starts, 1 mL of 25 mM $HAuCl_4$ was injected. After 30 minutes, the reaction was finished. After that, the sample was diluted by extracting 55 mL of sample (step 1) and adding 53 mL of ultrapure water and 2 mL of 60 mM sodium citrate. The resulting solution was then used as a seed solution to the next growing step, and the process was repeated (i.e. the dilution was heated until the boiling starts, and then 1 mL of 25 mM of $HAuCl_4$ was injected. After 30 minutes, the reaction was finished and 55 mL of sample (step 2) was extracted). In this way, a total of eleven growth steps were performed obtaining finally citrate-stabilized 95nm AuNPs (step 11).

For the resulting AuNPs, the molar gold concentration was estimated from the absorbance at 400 nm, which is assumed to have a size independent absorption coefficient.[16]

2.2. Material characterization. UV-visible spectra were recorded on a Cary 100 Bio UV-Vis spectrometer in disposable polystyrene cuvettes with 1.0 cm path length. Samples for transmission electron microscopy (TEM) were prepared by drying, under ambient conditions, a dispersion of the particles on 200 mesh copper grids coated with Formvar/Carbon film. TEM images were

obtained in a JEOL JEM 1400 TEM microscope, operated at an accelerating voltage of 80 kV. Powder X-ray diffraction (XRD) experiments were performing using a Bruker D8 ADVANCE diffractometer operating at 40 kV and 40 mA, and using Cu Kα radiation (1.5406 A).

2.3. Electrochemical experiments. Chronoamperometric, cyclic (CVs) and differential pulse (DPVs) voltammetric measurements were recorded on an AUTOLAB PGSTAT30 electrochemical analyzer using a three-electrode system. A glassy carbon (GC) disc (5 mm in diameter; Pine Instruments Company) were used as working electrodes. A drop of 25 μL of AuNPs sample (Au^0-concentration ~0.7 mM) was loaded onto the clean surface of GC electrode and then dried overnight at 4 ºC. A platinum sheet and an Ag/AgCl electrode were used as counter and reference electrodes, respectively. A 0.5 M KOH was used as supporting electrolyte. All the solutions were purged prior to electrochemical measurements using nitrogen (N_2) or oxygen (O_2) gas, depending on the experiment.

3. Results and Discussion.

Figure 1A shows the normalized spectra of each growth step of the citrate-stabilized AuNPs. The surface plasmon resonance (SPR) band maxima were located at 521, 525, 535, and 558 nm, respectively. The expected particle size values were *ca*. 18, 24, 52, and 96 nm, respectively.[16] The morphological characterization of the AuNPs was performed by TEM, see Figure 1B-E. The citrate-stabilized AuNPs were quasi-spherical in shape with a narrow distribution in size. Figure S1 shows the size-distribution histograms obtained from TEM images, demonstrating a good correlation with the theoretical sizes obtained from SPR bands. X-Ray diffraction (XRD) analysis was performed to confirm the crystalline structure of the resulting AuNPs. Figure 1F shows the XRD patterns for the four different growth steps on ITO support, which presented diffraction

patterns at 38.9°, 44.5°, 65°, and 77.7° corresponding to the (111), (200), (220), and (311) planes of a face centered cubic (fcc) structure, respectively. The latter Miller indices were almost identical to the given values in the standard JCPDS file 4-0784 of fcc Au.[18] Furthermore, as it was expected for larger crystalline nanomaterials, the relative intensity of the XRD peaks increase with the particle size.

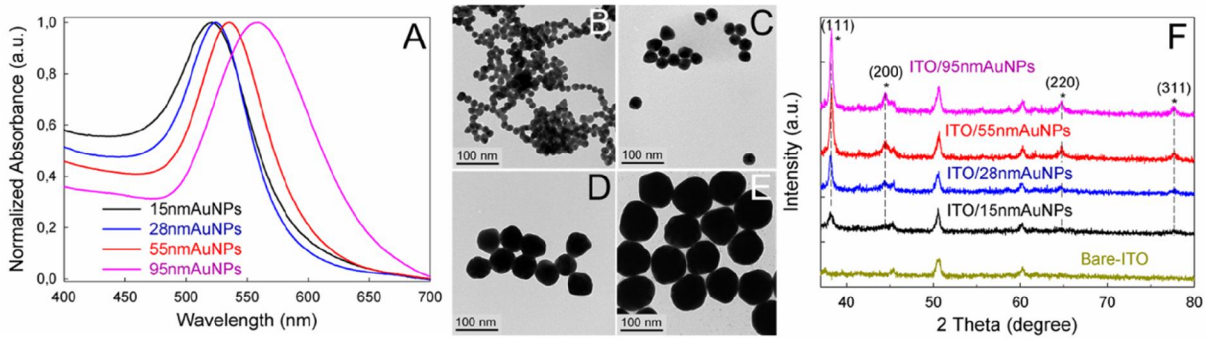

Figure 1. (A) UV-visible spectra and (F) XRD of citrate-stabilized AuNPs with different particle size. (B-E) TEM images of 15nm-(B), 28nm-(C), 55nm-(D), and 95nm-AuNPs (E).

To study the electrochemical behavior of the resulting citrate-stabilized AuNPs, they were deposited by drop-casting, and subsequent drying, on the surface of a glassy carbon electrode. First, the surface structure and the ratio of the existing facets on AuNPs of four different sizes were studied by lead underpotential deposition (Pb-UPD).[19] During the positive potential sweep, three stripping peaks corresponding to the desorption of lead layer on Au(111), (100) and (110) facets can be observed at around -0.7, -0.57 and -0.47 V, respectively (Figure 2). Overall, variations in the relative intensity of these three desorption peaks can be observed with the increase of the particle size. For instance, 15 nm AuNPs showed a single broad desorption peak, indicating that the most of their surface sites have (100) symmetry. Whilst, 95 nm AuNPs showed well-defined three domains (i.e. (111), (100) and (110)) with a similar relative intensity. These results suggest that citrate-stabilized 15 nm AuNPs are the best candidates as ORR electrocatalysts.

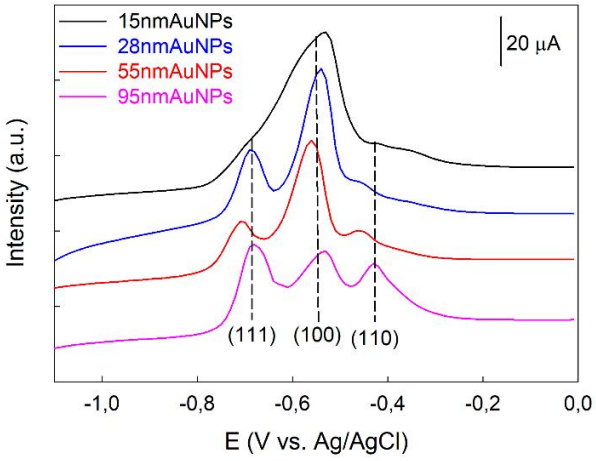

Figure 2. Desorption voltammetric profiles of the different AuNPs in 0.1 M NaOH and 1 mM $Pb(NO_3)_2$ recorded under N_2-saturated atmosphere. Scan rate: 20 $mV \cdot s^{-1}$.

Figure 3A,B displays the cyclic voltammograms (CVs) of the citrate-stabilized AuNPs in alkaline medium (0.5 M) saturated with N_2 and O_2, respectively. No electrochemical response within the potential ranges of -1.0 and -0.10 V in N_2-saturated solution was found, whereas well-defined cathodic peaks arise at -0.20 V in O_2-saturated conditions indicating the electrocatalytic effect of the citrate-stabilized AuNPs in oxygen reduction processes. Importantly, the intensities of the cathodic peaks as well as the onset potential of the O_2 reduction varied significantly with the size of the citrate-stabilized AuNPs, suggesting a clear dependence of the electrocatalytic activity with the nanoparticle size. These findings were supported by the differential pulse voltammograms (DPVs) of the AuNPs/GC electrodes in N_2- and O_2-saturated conditions (Figure 3C,D). In the absence of O_2, the resulting peaks were associated with the Au/AuOx redox process of the AuNPs. On the other hand, the peaks located between -0.20 and -0.38 V in the DPV curves correspond to the 2-electron oxygen reduction processes in the presence of O_2. The variation of the intensity values of the DPV curves clearly revealed a significant influence of the size of the

citrate-stabilized AuNPs on the ORR processes. Interestingly, the peaks located between -0.80 and -1.00 V correspond to ORR via 4-electron processes, showing the same core-size dependent tendency both for the potential and intensity values.

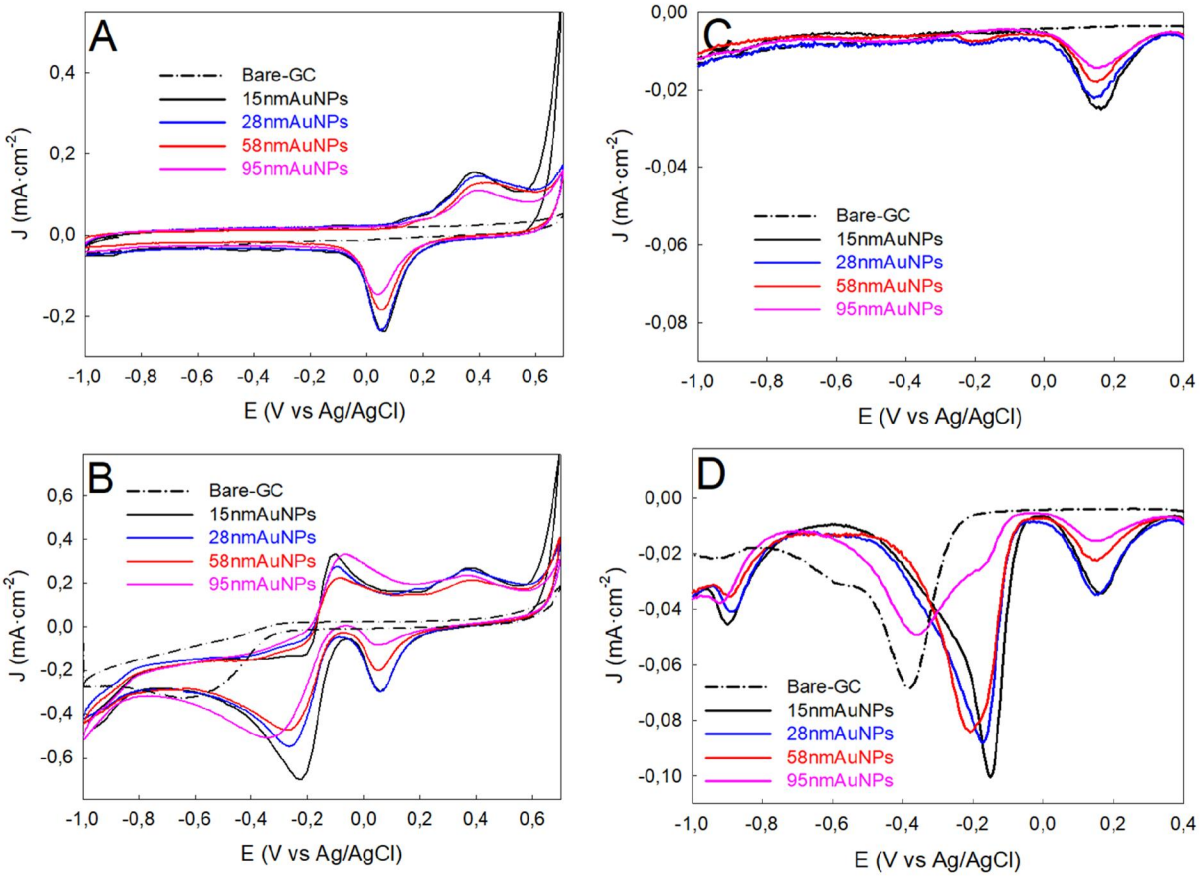

Figure 3. (A,B) Cyclic and (C,D) Differential Pulse voltammograms of GC electrodes modified with citrate-stabilized AuNPs of different particle size in N_2-saturated (A,C) and O_2-saturated 0.5 M KOH. Scan rate 0.1 $V \cdot s^{-1}$.

Further insights on the effect of citrate-stabilized AuNP core size on the electrocatalytic activity in ORR were pursued by analyzing the reaction kinetics properties by rotating-disk voltammetry. Note that the maximum current density values obtained at the initial forward scan were lower than those at the return scan during the rotating-disk voltammograms (RDVs), see Figure 4A. The

hysteresis might be attributed to the different interaction between Au surfaces and dioxygen in each scan. The dioxygen adsorption requires the displacement of the capping ligands on the Au surface during the initial forward scan, which might require a higher amount of energy than the one during the return scan. Probably, in the latter case, the oxygen adsorption is much favored because it requires the displacement of the reaction product (i.e. OH^- or HO_2^-).[20] Figure 4B demonstrates that the same value of maximum current density obtained during the return scan of the CV was achieved applying a constant potential of −1.0 V, see Figure 2B. Thus, the latter result validates the use of return scan for the following kinetic analysis. Figure S2 compares the hysteresis effect on ORR for the different citrate-stabilized AuNPs, showing clear size dependence.

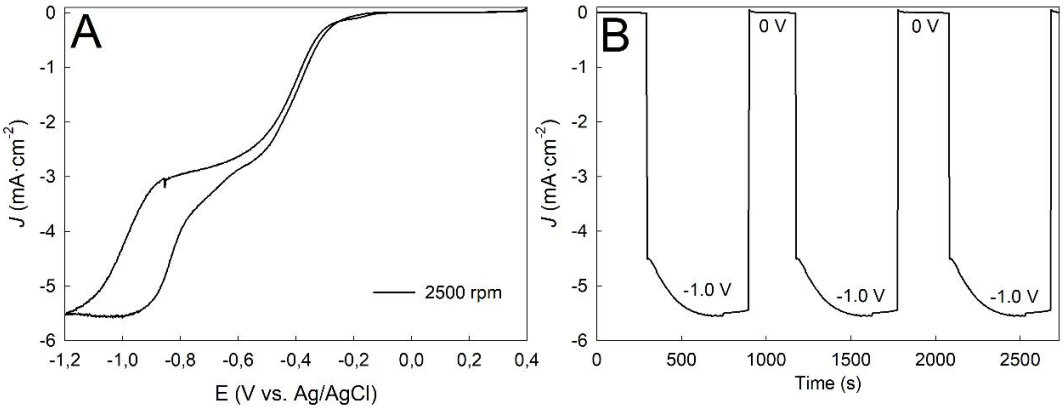

Figure 4. Hysteresis effect during measurements with rotating disk electrode: (A) Rotating-disk voltammograms and (B) Cronoamperograms of GC/15nmAuNPs electrode at rotating rate of 2500 rpm in O_2-saturated 0.5 M KOH. Scan rate 10 $mV \cdot s^{-1}$.

In order to further understand the latter mentioned hysteresis effect on AuNPs-based electrocalysts toward ORR reaction, two types of dynamic experiments were carried out using rotating-disc electrode modified with citrate-stabilized 15 nm AuNPs (Figure S3). The first

experiment was performed by decreasing the amount of citrate-stabilized 15 nm AuNPs deposited on the surface of the GC electrode (Figure S3A-D), and the second one, shortening the initial potential applied during the cyclic voltammetry measurements (Figure S3D,E). These results demonstrated that, at least, the hysteresis effect is a process dependent both on the amount of electrocatalyst deposited on the surface of GC electrode and on the range of applied potential during the voltammetric measurements.

Figure 5A shows the comparative rotating-disk voltammograms (RDVs) for ORR of the four different AuNPs/GC electrodes at the same rotating rate of 2500 rpm. On the one hand, the maximum current density at -1.0 V increased with decreasing the particle size, obtaining values of -5.58, -5.08, -4.47 and -3.71 $mA \cdot cm^{-2}$ for 15nm-, 28nm-, 55nm- and 95nm-AuNPs/GC electrodes, respectively. A clear core-size dependence can be observed, in agreement with our previous CVs and DPVs analysis. This dependence can be attributed to the comparatively higher surface area of the smaller AuNPs. Noticeably that the limiting current density obtained for our citrate-stabilized 15nmAuNPs/GC electrode at 2500 rpm was the maximum possible value following a four-electron pathway and considering the geometrical area of the GC working electrode.[21] It is a clear evidence of the suitability as electrocatalyst for the ORR of the citrate-stabilized 15nmAuNPs.

The onset potential values of ORR shift negatively with the increase of the AuNP size, see Table 1. Note that the same onset value (*i.e.* -0.20 V) is obtained for citrate-stabilized 15nmAuNPs/GC and $Au_{55}Cl_6(PPh_3)_{12}$ clusters.[22] These interesting results can be attributed to the different capped ligands, which can block catalytically active sites of metal NPs and lower the catalytic activity.[23] Therefore, the electrostatically adsorbed citrate ligand appears as a much more suitable ligand for oxygen adsorption than covalently bound tiol- and tertiary phosphine- binding ligands.

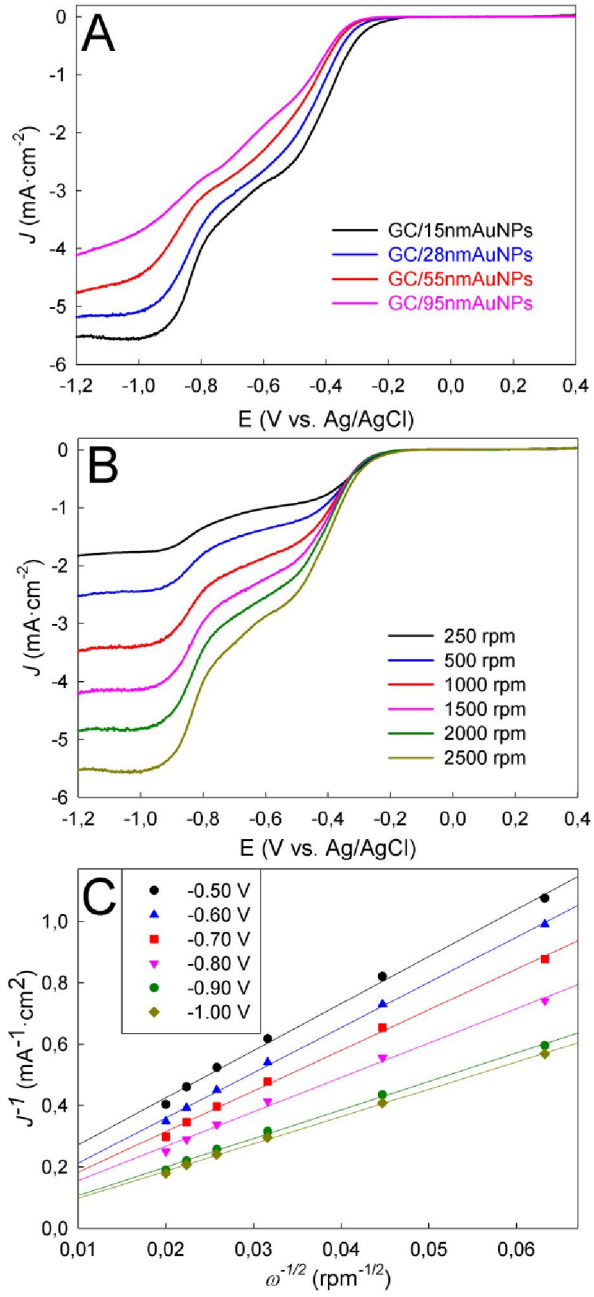

Figure 5. (A) Rotating-disk voltammograms (RDVs) of GC electrodes modified with citrate-stabilized AuNPs of different particle size at same rotating rate of 2500 rpm, and (B) RDVs for a GC/15nmAuNPs modified electrode at different rotation rates, in O_2-saturated 0.5 M KOH. Scan rate 10 $mV \cdot s^{-1}$. (C) Koutecky-Levich plots at different electrode potentials obtained from (B).

Table 1. Kinetic parameters for ORR of the GC electrodes modified with citrate-stabilized AuNPs of different particle size. The onset potential values were determined from rotating-disk voltammograms (Figure 3A).

	15nmAuNPs	**28nmAuNPs**	**55nmAuNPs**	**95nmAuNPs**
Onset potential (V)	-0.20	-0.24	-0.28	-0.30
Number of electrons transferred at -0.50 V	2.36	2.34	2.68	2.01
J_K at -0.50 V (mA·cm^{-2})	-8.33	-5.11	-2.95	-2.55
k (cm·s^{-1}) at -0.50 V	0.035	0.022	0.011	0.012
Number of electrons transferred at -1.00 V	4.07	4.08	3.92	3.56
J_K at -1.00 V (A·cm^{-2})	-115.2	-43.97	-21.25	-12.64
k (cm·s^{-1}) at -1.00 V	0.285	0.108	0.054	0.035

Figure 5B shows the resulting RDVs for 15nmAuNPs/GC electrode at different rotation rates from 2500 to 250 rpm. The shape of our curves was similar to the one reported previously for 1 nm Au thin film/GC electrode prepared by vacuum evaporation of gold at a base pressure of $2 \cdot 10^{-6}$ Torr, requiring a rotation rate of 4600 rpm for obtaining a similar limiting current density at -1.0 V (*i.e.* -5.58 mA·cm^{-2}).[24] RDV was applied to citrate-stabilized AuNPs of different sizes; see Figure S4 and Table 1:

$$\frac{1}{J} = \frac{1}{J_L} + \frac{1}{J_K} = \frac{1}{B\omega^{1/2}} + \frac{1}{J_K} \qquad (1)$$

$$B = 0.62nFC_0D_0^{2/3}v^{1/6} \qquad (2)$$

$$J_K = nFkC_0 \qquad (3)$$

where J is the measured current density, J_K and J_L are the kinetic and diffusion limiting current densities, respectively, ω is the electrode rotation rate, n is the overall number of electrons transferred in oxygen reduction, F is the Faraday constant, C_0 is the bulk concentration of O_2 dissolved in the electrolyte ($1.03 \cdot 10^{-3}$ mol·L^{-1} for 0.5 M KOH), D_0 is the diffusion coefficient of O_2 ($1.63 \cdot 10^{-5}$ cm^2·s^{-1} for 0.5 M KOH), v is the kinematic viscosity of the electrolyte (0.01 cm^2·s^{-1} for 0.5 M KOH), and k is the electron transfer rate constant during ORR.[25]

Figure 5C shows the Koutecky–Levich (K-L) plot obtained from the RDVs of the 15nmAuNPs/GC electrode. The excellent linearity of the experimental points demonstrates a first-order reaction kinetic toward dissolved O_2. According to equations (1) and (2), the values of J_K and n can be obtained from the slope and intercept of this *K-L* plot, respectively. The rate constants (k) were estimated using the equation (3). Table 1 summarized the resulting kinetic parameters of our 4 different AuNPs/GC electrodes, both at -0.50 V and at -1.00 V. Overall, the ORR was found to proceed by a four-electron reaction pathway at -1.00 V, while at -0.50 V the ORR was performed by a two-electron reaction route. In other words, depending of the applied potential, the formation of OH^- or HO_2^- as byproduct of the ORR can be conveniently controlled.[26] Therefore, the present concept of potential-dependent electrocatalyst using exclusively citrate-stabilized AuNPs/GC electrode could be extrapolated to other reduction reactions and improve the control of product selectivity in electrocatalytic processes.

Finally, the stability of citrate-stabilized 15 nm AuNPs was evaluated using an accelerated aging test (AAT), which uses thousand scanned potential performed by cyclic voltammetries in oxygen-saturated 0.1 M KOH solution.[27,28] Figure S5 shows that, after ATT, the ORR onset- and peak-potential associated with 2 electrons transfer pathway were negatively shifted by 92 mV, while these same parameters were positively shifted by 170 mV for the 4 electrons transfer pathway.

Moreover, the peak current densities for both ORR mechanisms have clearly increased after ATT, indicating a possible activation process of this type of Au-electrocatalyst. Furthermore, these results clearly demonstrated its excellent suitability as ORR electrocatalyst in alkaline electrolyte.

4. Conclusions.

The nano-size effect on the electrocatalytic properties of citrate-stabilized AuNPs for ORR has been assessed. The proposed nanoelectrocatalysts were synthesized by a green and scaled-up synthesis method. The particle size of the citrate-stabilized AuNPs influences the maximum current density and the onset potential values, being two relevant parameters in the quantitative assessments of electrocatalytic performance. The citrate-stabilized AuNPs render a comparable electrocatalytic performance to those reported for Au-clusters. This work highlights the crucial role of the capping ligands coating the Au-core even for Au nanoclusters. Therefore, our work paves the way for ligand-oriented and surface chemistry design of highly efficient nanomaterials for electrocatalysis of the ORR. We consider that our findings may remarkably impact their possible application in fuel cell technology, where the high cost of the electrocatalyst is one of the critical aspects.

Supporting Information Description. Size-distribution histograms obtained from the TEM images for each growth step, additional rotating-disk voltammograms and the AAT. The following files are available free of charge Supporting Information (PDF).

Acknowledgment. Support from the Ministry of Economy and Competitiveness of Spain is acknowledged through the CTQ2017-83961-R project. J.J.G.-C. acknowledges the Ministry of Economy and Competitiveness for a “Ramon y Cajal” contract (#RyC-2014-14956). M. C. thanks

the “Plan Propio de Investigación” from the Universidad de Córdoba (UCO) and the “Programa Operativo de fondos FEDER Andalucía” for its financial support through a postdoctoral contract (Modality 5.2.A). The publication has been prepared with support from RUDN University Program 5-100. Rafael Luque gratefully acknowledges MINECO for funding project CTQ2016-78289-P, co-financed with FEDER funds. Alain R. Puente-Santiago gratefully acknowledge MINECO for their research contracts associated to the aforementioned project, and to the Research Program of the UCO for its financial support through a postdoctoral contract (Modality 5.1). They also thank Prof. Dr. J. M. Rodríguez-Mellado of the Department of Physical Chemistry and Applied Thermodynamics at the UCO for kind access to the rotating disk equipment.

References

(1) Liu, L.; Corma, A. Metal Catalysts for Heterogeneous Catalysis: From Single Atoms to Nanoclusters and Nanoparticles. *Chem. Rev.* **2018**, *118* (10), 4981–5079.

(2) Fei, H.; Dong, J.; Feng, Y.; Allen, C. S.; Wan, C.; Volosskiy, B.; Li, M.; Zhao, Z.; Wang, Y.; Sun, H.; et al. General Synthesis and Definitive Structural Identification of MN4C4 Single-Atom Catalysts with Tunable Electrocatalytic Activities. *Nat. Catal.* **2018**, *1* (1), 63–72.

(3) Rück, M.; Bandarenka, A.; Calle-Vallejo, F.; Gagliardi, A. Oxygen Reduction Reaction: Rapid Prediction of Mass Activity of Nanostructured Platinum Electrocatalysts. *J. Phys. Chem. Lett.* **2018**, *9* (15), 4463–4468.

(4) Liu, K.; Zhang, C.; Sun, Y.; Zhang, G.; Shen, X.; Zou, F.; Zhang, H.; Wu, Z.; Wegener, E. C.; Taubert, C. J.; et al. High-Performance Transition Metal Phosphide Alloy Catalyst for Oxygen Evolution Reaction. *ACS Nano* **2018**, *12* (1), 158–167.

(5) Wu, J.; Yang, H. Platinum-Based Oxygen Reduction Electrocatalysts. *Acc. Chem. Res.* **2013**, *46* (8), 1848–1857.

(6) Xia, B. Y.; Yan, Y.; Li, N.; Wu, H. Bin; Lou, X. W. (David); Wang, X. A Metal–organic Framework-Derived Bifunctional Oxygen Electrocatalyst. *Nat. Energy* **2016**, *1* (1), 15006.

(7) Wan, L.; Qin, Y.; Xiang, J. Rapid Electrochemical Fabrication of Porous Gold Nanoparticles for High-Performance Electrocatalysis towards Oxygen Reduction. *Electrochim. Acta* **2017**, *238*, 220–226.

(8) Seselj, N.; Engelbrekt, C.; Ding, Y.; Hjuler, H. A.; Ulstrup, J.; Zhang, J. Tailored Electron Transfer Pathways in Au Core /Pt Shell-Graphene Nanocatalysts for Fuel Cells. *Adv. Energy Mater.* **2018**, *8* (13), 1702609.

(9) Wang, L.; Tang, Z.; Yan, W.; Yang, H.; Wang, Q.; Chen, S. Porous Carbon-Supported Gold Nanoparticles for Oxygen Reduction Reaction: Effects of Nanoparticle Size. *ACS Appl.*

Mater. Interfaces **2016**, *8* (32), 20635–20641.
(10) Yi, J.-D.; Xu, R.; Wu, Q.; Zhang, T.; Zang, K.-T.; Luo, J.; Liang, Y.-L.; Huang, Y.-B.; Cao, R. Atomically Dispersed Iron–Nitrogen Active Sites within Porphyrinic Triazine-Based Frameworks for Oxygen Reduction Reaction in Both Alkaline and Acidic Media. *ACS Energy Lett.* **2018**, *3* (4), 883–889.
(11) Chakraborty, S.; Babanova, S.; Rocha, R. C.; Desireddy, A.; Artyushkova, K.; Boncella, A. E.; Atanassov, P.; Martinez, J. S. A Hybrid DNA-Templated Gold Nanocluster For Enhanced Enzymatic Reduction of Oxygen. *J. Am. Chem. Soc.* **2015**, *137* (36), 11678–11687.
(12) Lalaoui, N.; Rousselot-Pailley, P.; Robert, V.; Mekmouche, Y.; Villalonga, R.; Holzinger, M.; Cosnier, S.; Tron, T.; Le Goff, A. Direct Electron Transfer between a Site-Specific Pyrene-Modified Laccase and Carbon Nanotube/Gold Nanoparticle Supramolecular Assemblies for Bioelectrocatalytic Dioxygen Reduction. *ACS Catal.* **2016**, *6* (3), 1894–1900.
(13) Zhou, Y.; Zeng, H. C. Metal–Hydroxide and Gold–Nanocluster Interfaces: Enhancing Catalyst Activity and Stability for Oxygen Evolution Reaction. *J. Phys. Chem. C* **2016**, *120* (51), 29348–29357.
(14) Seitz, L. C.; Hersbach, T. J. P.; Nordlund, D.; Jaramillo, T. F. Enhancement Effect of Noble Metals on Manganese Oxide for the Oxygen Evolution Reaction. *J. Phys. Chem. Lett.* **2015**, *6* (20), 4178–4183.
(15) Sumner, L.; Sakthivel, N. A.; Schrock, H.; Artyushkova, K.; Dass, A.; Chakraborty, S. Electrocatalytic Oxygen Reduction Activities of Thiol-Protected Nanomolecules Ranging in Size from Au 28 (SR) 20 to Au 279 (SR) 84. *J. Phys. Chem. C* **2018**, *122* (43), 24809–24817.
(16) Bastús, N. G.; Comenge, J.; Puntes, V. Kinetically Controlled Seeded Growth Synthesis of Citrate-Stabilized Gold Nanoparticles of up to 200 Nm: Size Focusing versus Ostwald Ripening. *Langmuir* **2011**, *27* (17), 11098–11105.
(17) Alba-Molina, D.; Rodríguez-Padrón, D.; Puente-Santiago, A.R.; Giner-Casares, J.J.; Martín-Romero, M. T.; Camacho, L.; Martins, L. O.; Muñoz-Batista, M. J.; Cano, M.; Luque, R. Mimicking the bioelectrocatalytic function of recombinant CotA laccase via electrostatically self-assembled nanobioconjugates. Nanoscale 2018, DOI: 10.1039/C8NR06001K.
(18) Turkevich, J.; Kim, G. Palladium: Preparation and Catalytic Properties of Particles of Uniform Size. *Science* **1970**, *169* (3948), 873–879.
(19) Hernández, J.; Solla-Gullón, J.; Herrero, E.; Aldaz, A.; Feliu, J.M. Electrochemistry of Shape-Controlled Catalysts: Oxygen Reduction Reaction on Cubic Gold Nanoparticles. *J. Phys. Chem. C* **2007**, *111* (38), 14078-14083.
(20) Rizo, R.; Arán-Ais, R. M.; Padgett, E.; Muller, D. A.; Lázaro, M. J.; Solla-Gullón, J.; Feliu, J. M.; Pastor, E.; Abruña, H. D. Pt-Rich Core /Sn-Rich Subsurface /Pt Skin Nanocubes As Highly Active and Stable Electrocatalysts for the Ethanol Oxidation Reaction. *J. Am. Chem. Soc.* **2018**, *140* (10), 3791–3797.
(21) Xing, W.; Yin, G.; Zhang, J. *Rotating Electrode Methods and Oxygen Reduction Electrocatalysis*; Elsevier: Amsterdam, Netherlands, 2014.
(22) Chen, W.; Chen, S. Oxygen Electroreduction Catalyzed by Gold Nanoclusters: Strong Core Size Effects. *Angew. Chemie Int. Ed.* **2009**, *48* (24), 4386–4389.
(23) Cao, Z.; Zacate, S. B.; Sun, X.; Liu, J.; Hale, E. M.; Carson, W. P.; Tyndall, S. B.; Xu, J.;

Liu, X.; Liu, X.; et al. Tuning Gold Nanoparticles with Chelating Ligands for Highly Efficient Electrocatalytic CO_2 Reduction. *Angew. Chemie Int. Ed.* **2018**, *57* (39), 12675–12679.

(24) Sarapuu, A.; Nurmik, M.; Mändar, H.; Rosental, A.; Laaksonen, T.; Kontturi, K.; Schiffrin, D. J.; Tammeveski, K. Electrochemical Reduction of Oxygen on Nanostructured Gold Electrodes. *J. Electroanal. Chem.* **2008**, *612* (1), 78–86.

(25) Mukherjee, D.; P, M. A.; Sampath, S. Few-Layer Iron Selenophosphate, FePSe 3 : Efficient Electrocatalyst toward Water Splitting and Oxygen Reduction Reactions. *ACS Appl. Energy Mater.* **2018**, *1* (1), 220–231.

(26) Hernández, J.; Solla-Gullón, J.; Herrero, E.; Aldaz, A.; Feliu, J. M. Characterization of the Surface Structure of Gold Nanoparticles and Nanorods Using Structure Sensitive Reactions. *J. Phys. Chem. B* **2005**, *109* (26), 12651–12654.

(27) Guo, C.; Liao, W.; Li, Z.; Sun, L.; Chen, C. Easy conversion of protein-rich enoki mushroom biomass to a nitrogen-doped carbon nanomaterial as a promising metal-free catalyst for oxygen reduction reaction. *Nanoscale* **2015**, *7*, 15990-15998.

(28) Franco, A.; Cano, M.; Giner-Casares, J. J.; Rodríguez-Castellon, E.; Luque, R.; Puente Santiago, A. R. Boosting electrochemical oxygen reduction activity of hemoglobin onto fructose@graphene-oxide nanoplatforms. *Chem. Commun.* **2019**, DOI: 10.1039/C9CC01625B.

Table of Contents (TOC) Image